Rotational snap-through behavior of multi-stable beam-type metastructures

Zhang, Yong; Tichem, Marcel; Keulen, Fred van

DOI
10.1016/j.ijmecsci.2020.106172

Publication date
2021

Document Version
Final published version

Published in
International Journal of Mechanical Sciences

International Journal of Mechanical Sciences 193 (2021) 106172

Contents lists available at ScienceDirect

International Journal of Mechanical Sciences

journal homepage: www.elsevier.com/locate/ijmecsci

Rotational snap-through behavior of multi-stable beam-type metastructures

Yong Zhang*, Marcel Tichem, Fred van Keulen

Department of Precision and Microsystems Engineering, Delft University of Technology, Mekelweg 2, Delft, 2628 CD, The Netherlands

ARTICLE INFO

Keywords:
Metastructure
Snapping beam
Multi-stability
Rotational state

ABSTRACT

Metastructures consisting of planar arrangements of bi-stable snap-through beams are able to exhibit multiple stable configurations. Apart from the expected translational state transition, when all beam elements snap through, rotational states may exist as well. In this paper we explore the rotational properties of multi-stable metastructures on the basis of both experimental and theoretical investigations, and define the conditions for achieving rotational stable states. Results show that the metastructure is able to realize both translational and rotational states, while the rotational transitions require less energy as compared to their translational counterparts. The influence of geometric parameters on rotational stability is investigated via parametric studies. Furthermore, to determine the design criteria for rotational stability, a theoretical investigation based on mode superposition principle is performed to predict the nonlinear-deformation of a unit cell. The theoretical analysis predicts well the rotational snap-through transitions that are observed in finite element simulations. It is found that the rotational stability is determined by setting proper values for h/L and t/L (h, t, L represent apex height, thickness and span of the bi-stable beam structure, respectively). Finally, we experimentally demonstrate that the proposed metastructure with multiple layers is able to achieve large rotations and translations.

1. Introduction

The design of mechanical metastructures is a rapidly emerging field, because of the potential to create unusual mechanical properties, such as ultra-high stiffness but lightweight [1–5], negative Poisson's ratio [6–8], and negative thermal expansion [9–13]. These superior features are mainly realized by the rational design of their unit structures. For example, arranging unit cells in a re-entrant pattern can result in a negative Poisson's ratio of the macroscopic metastructure [14]. At present, a variety of mechanical metastructures have been proposed and intensively studied for various applications, including medical implants [15,16], soft robots [17,18], and microelectromechanical systems [19].

More recently, the strategy of utilizing buckling, which is generally avoided in classical structural designs, has been extensively reported in metastructural design [20–24]. The designed instability-based mechanical metastructures allow for large macroscopic deformations with recoverable shape changes, and thus they are also referred to as reconfigurable metastructures [25–28]. New functionalities, e.g. tuneable mechanical behavior, can be achieved by such metastructures. However, these transformations of geometry or reconfiguration usually require continuous power, in the sense that a continuous external actuation is necessary to maintain the deformed configuration. One way to improve energy efficiency is to introduce bi- or multi-stability, so that a structure maintains different states without the need for continuous energy supply. In designing such multi-stable metastructures, pre-shaped beams have been commonly adopted as basic elements since they have large loading-bearing capacity and can be easily manufactured via additive manufacturing [21,29]. When an applied load reaches a critical level, the beam will jump from one configuration into another configuration, which is referred to as snap-through behavior [30]. By arranging multiple snapping beams, the associated metastructures are able to exhibit multiple self-stable configurations. Many examples of regularly assembled pre-shaped beams in one or two dimensions (1D or 2D), referred to as multi-stable beam-type metastructures (MBMs), can be found in literature [31–39].

In light of the stacking of the snapping beams with two stable configurations, MBMs are normally capable of achieving a large reversible switching motion, which has been utilized for energy absorption [40–43]. It has been demonstrated that the multi-stability can enhance the ability of reducing peak acceleration while MBMs are still reusable [44]. In addition, such MBMs, as reconfigurable structures, can be widely used for designing motion-driven mechanisms including deployable structures, shape-changing structures, actuators, soft robotics, and motion systems [45–50]. These motion-driven applications usually require multiple degrees of freedom and the monolithic multi-stable structures might offer a compact solution for such challenges. For instance, Chen et al. [45] presented a design for propulsion of soft robots, exploiting motions from the snapping of beams. Santer et al. [47] ex-

* Corresponding author.
E-mail address: Y.Zhang-15@tudelft.nl (Y. Zhang).

https://doi.org/10.1016/j.ijmecsci.2020.106172
Received 3 June 2020; Received in revised form 10 October 2020; Accepted 24 October 2020
Available online 29 October 2020

ploited 1D translational motion of a multi-stable structure to deploy a surface. Pontecorvo et al. [48] proposed the concept of using bi-stable elements to extend a helicopter rotor blade, based on the large translation of MBMs. Besides, Che et al. [51] designed a multi-stable beam-type structure using different materials for each layer to control its deformation sequences. The dynamic behavior of MBMs was also investigated to analyze its vibration modes [52]. However, most proposed MBMs are limited in terms of allowable directions and are only presented with their translational motions. Their potential to realize rotational stable states has not been revealed and studied, and thus this limits their feasibility in motion-driven applications where rotational movements are typically needed, such as actuators, deployable structures and robotics.

To enrich multi-stable structure's reconfiguration capability, in this work we explore the possibility for MBMs to achieve rotational movements. This paper aims to analyze the rotational behavior of MBMs and study design conditions for structures to realize additional rotational states. Although previous papers on MBMs give important insights into the mechanics of the translational transitions, the potential of rotational reconfiguration is restricted in most previous designs and little information is available on the rotational stability of MBMs. In this paper, the rotational behavior of MBMs is characterized via experimental and numerical approaches, and the design requirements for rotational states are investigated via an analytical model, which can rapidly identify the design space for the rotational stability. The resulting multi-stable structures exhibit both translational and rotational motions, which can further enhance multi-stable mechanisms' deployment capacities. For instance, the rotational transitions can be exploited to design multi-stable bending actuators in which rotational degrees of freedom are essential, while the intrinsic translational state can be harnessed to provide extensions or contractions.

The remainder of this paper is organized as follows. Section 2 describes the structural geometry of MBMs and methods we use in this work. The mechanical properties and resulting rotational stable states are characterized experimentally and numerically via a parametric study, as presented in Section 3. In Section 4, we conduct a theoretical analysis to investigate the rotational stability. Section 5 describes the mechanical behavior of multi-layer metastructures exhibiting large rotations and translations. Conclusions are presented in Section 6.

2. Structural design and methods

2.1. Structural geometry and stable states

The structural design of MBMs studied in this paper is based on the snap-through behavior of curved beams, which were first studied by Vangbo et al. [53]. In this paper, pre-shaped curved beams are used as basic elements to construct multi-stable metastructures, as shown in Fig. 1. Each beam element illustrated in Fig. 1(b) is composed of a curved beam, upper and lower frame (marked in blue). The geometric parameters of the frames are shown in the inset table and are fixed in this study. The original shape ($w_0(x)$) of the curved beam illustrated in Fig. 1(b) can be expressed as:

$$w_0(x) = \frac{h}{2}\left(1 - cos(2\pi\frac{x}{L})\right) \tag{1}$$

where h and L represent initial beam height and length, respectively. The beam's in-plane thickness and out-of-plane thickness are denoted as t and b, respectively. These three parameters (h, L, and t) are considered as design parameters and their influence on rotational behavior is systematically discussed in this paper. As illustrated in Fig. 1(a), by serially combining multiple beam elements, MBMs can be designed.

The resulting metastructures and their stable states are demonstrated in Fig. 1(c), where the representative unit is referred to as a unit cell that consists of two beam elements: left and right beam element, as denoted in the figure. The unit cell can deform into flat or tilted stable configurations. These flat and tilted stable configurations are referred to as translational and rotational states respectively in the remainder of this paper. The unit cell possesses four stable configurations: the initial state and three deformed stable states including one translational and two rotational stable states. When the unit cell switches from the initial to the translational state, both beams undergo the same deformations and snap to the second stable state. Therefore, the behavior of translational transitions can be obtained based on a study for one side, either the left or right beam element. However, symmetry breaks up during the transition to the rotational state, where both curved beams deform with different manners. In particular, the left beam element snaps while the right beam element is mainly rotated. The resulting rotational state is enabled by a collective effect of the left beam element's snapping deformations and rotational deformations of right beam element. Consequently, me-

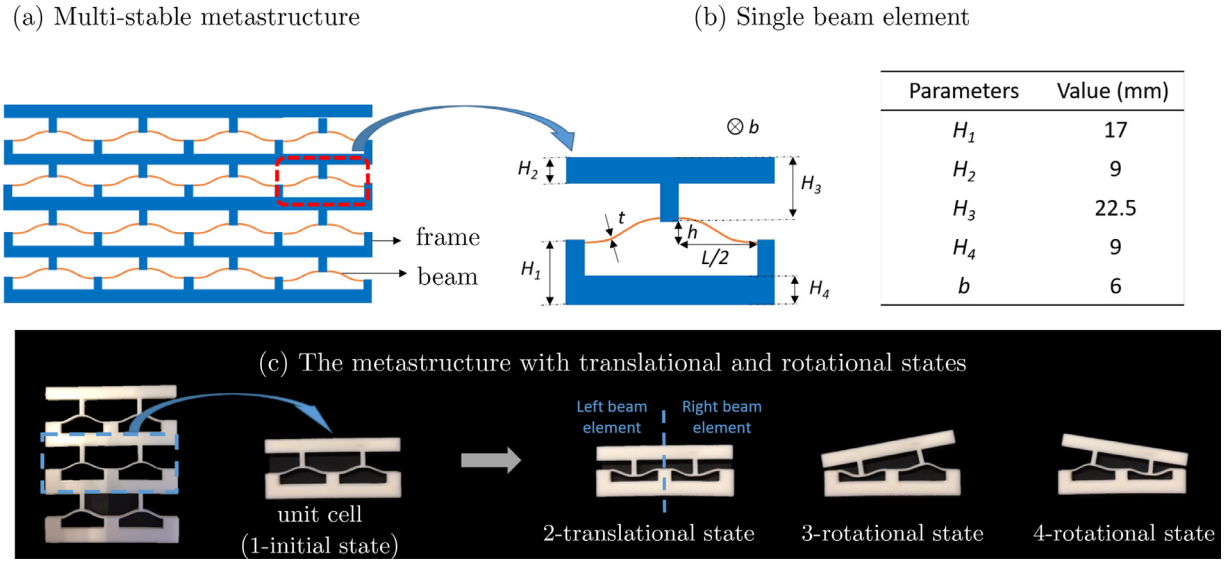

Fig. 1. A demonstration of multi-stable structures with translational and rotational stable states. (a) A schematic for the proposed multi-stable metastructure. The structure is designed by serially stacking curved beams with thick frames. (b) Geometric parameters of the beam element are depicted. The out-of-plane dimension is denoted as b. (c) Each unit cell ($h = 5$ mm $t = 0.8$ mm and $L = 28$ mm) possesses four stable states such that it can snap into the translational state or the rotational states.

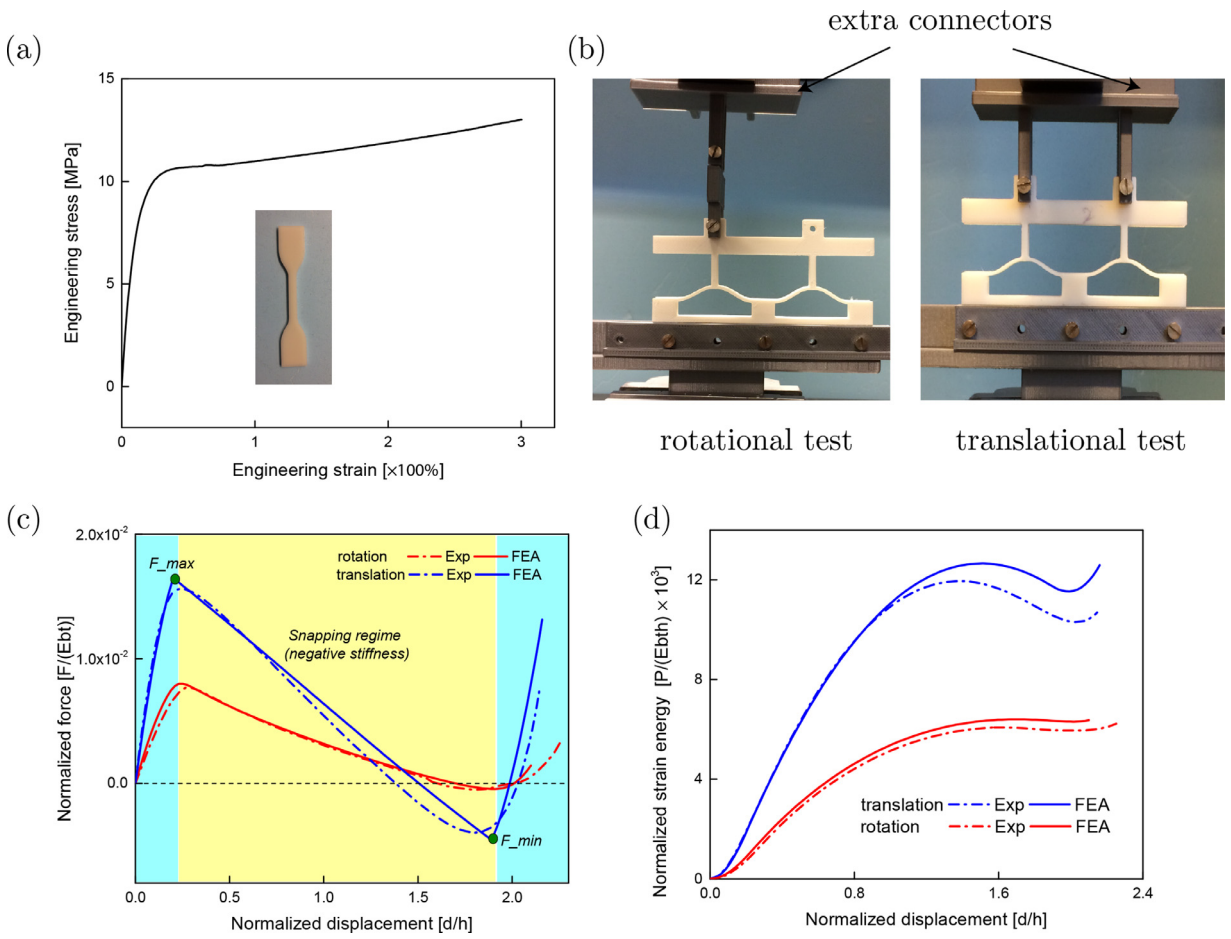

Fig. 2. Characterization of snap-through transitions of the unit cell. (a) Stress-strain results for the material we used. (b) Experimental setup for measuring rotational (left) and translational (right) transitions. Samples are clamped at the bottom and connected to the printed part at the top. (c) Normalized load-displacement curves of snap-through transitions. The blue regions represent positive stiffness phases while the yellow area stands for the snapping phase, exhibiting negative stiffness. F_{max} and F_{min} represent the maximal and minimal force of each load-deflection curves, respectively. (d) Evolution of the normalized strain energy of the unit cell during the uniaxial loading.

chanics and design requirements for the proposed rotational state are different from that of translational transitions. To establish the design criteria for reaching rotational states, an analytical study is performed in Section 4.

2.2. Fabrication and experimental tests

To study the proposed multi-stable metastructures' behavior, a series of samples were fabricated via a fused deposition printer using flexible thermoplastic polyurethanes (TPU, Flex-45, RS). TPU is an environmental friendly material with advantages of good wear resistance and large recoverable elastic strains. Its properties were characterized by standard tensile measurements according to ASTM D638-14 [40]. The measured Young's modulus (E) and Poisson's ratio (ν) are 95 MPa and 0.4, respectively. The corresponding stress-strain curve is plotted in Fig. 2(a).

Uniaxial loading tests were conducted to characterize metastructures' snap-through transitions as load-displacement curves. Quasi-static loading conditions were applied using a universal testing system (Zwick-Roell Z005) with a loading rate of 10 mm/min in a displacement-control manner. For each sample, multiple tests were conducted to get average load-displacement curves. Extra parts used for connecting samples to the testing system were designed and printed using polylactic acid (PLA), as seen in Fig. 2(b). To allow for unit cells' rotations during uniaxial testing, two rigid parts were assembled using screws to mimic hinge connections. Loads were applied on one side of the frame. For characterizing translational motions, clamped conditions were applied between specimens and the extra parts, as displayed in Fig. 2(b).

2.3. Numerical methods

Finite element models were established by using software ABAQUS/Standard (2017) to examine the structures' mechanical behavior, where geometric parameters are in accordance with those of experiments. A Marlow hyper-elastic material model was adopted as a constitutive relation in finite element analysis (FEA) [54]. Here, the stress-strain curve shown in Fig. 2(a) was imported to ABAQUS. Eight-node brick elements (C3D8) were used to mesh the structure geometry, with mesh convergence analysis performed to ensure accuracy. Nonlinear geometric FEA based on static/general procedure was conducted by prescribing vertical displacements at specific loading points on the top of the unit cell, which is consistent with the experimental compression tests shown in Fig. 2(b). The bottom of the structure is fully fixed in x, y, z directions. The reaction forces were collected in each iteration from nodes where vertical displacements were applied.

3. Mechanical response for rotational transitions

In this section, we characterize the rotational transitions of the representative element, which is the unit cell defined before. Moreover, a parametric study is performed to investigate the influence of primary geometric parameters.

3.1. Characteristics of snap-through behavior

The force and vertical displacement of loading points shown in Fig. 2(b) are denoted as F and d, respectively. The measured force and displacement are then normalized by Ebt and h, respectively. Fig. 2(c) shows force-displacement curves for translational and rotational snap-through behavior. It can be observed that there is a good quantitative agreement between experimental and numerical results. Negative stiffness is captured in both translational and rotational transition curves. The force first gradually increases along with the displacement and then instability (i.e. snapping) is triggered when reaching the maximum force (denoted as F_{max}). Under force-control loading condition, snap-through behavior typically exhibits "displacement jump" after reaching F_{max}. In this work we apply displacement-control loading condition to capture the full force-displacement curve shown in Fig. 2(c), with a negative stiffness phase (the yellow region in the figure). In this paper, we refer to this negative stiffness phase as snap-through transitions. F_{min} represents the minimum force in the force-displacement curve. In this figure, the magnitude of F_{max} for translation is approximately two times larger than for rotation. This is due to the fact that in case of translational transitions, two beams undergo bending and compression deformations, while for the case of rotations mainly the beam near the loading position deforms. Moreover, the minimum force F_{min} for translation is also higher than for rotations as a result of deformations of two beams. This implies that recovering from the translational to the initial state needs larger force as compared to reversing the rotational state. In addition, we assess the symmetry of snap-through transition by defining a quantity $\eta = |F_{max}/F_{min}|$. When η is close to 1, the structure intends to exhibit symmetric transitions. Here, the η for translational transitions in Fig. 2(c) is 3.95, whereas the counterpart of rotational curve is 15.24. This indicates that the unit cell's rotational deformation exhibits a more evident asymmetric characteristic as compared to translational deformations. The highly asymmetric behavior of rotations is attributed to two aspects: the snapping deformation of the left beam element and rotational deformations of the right beam element, as discussed in Section 2.1.

The evolution of strain energy (P) during the loading process is shown in Fig. 2(d). P is equal to the area under the corresponding force displacement curve. It indicates that both the translational and rotational state transitions exhibit a local minimum in the energy landscape, which correspond to the deformed (translational and rotational) stable states. The rotational snap-through (negative stiffness) can be understood as: by applying prescribed displacements as shown in Fig. 2(b), the right beam element is mainly bent. The left beam element experiences bending and compression deformations, where the compression energy first increases and then decreases, leading to the decline of the unit cell's strain energy. In addition, it can be observed that the energy of deformed stable state is larger than that of the initial undeformed state, which implies a sufficiently large disturbance may cause the structure to switch back to its initial state that has a lower potential energy.

3.2. Influence of geometric parameters on rotational states

For multi-stable metastructures, tuning geometric parameters can result in different mechanical properties including strength, stiffness and stability. Rotational behavior of these metastructures is mainly controlled by the beams' geometric parameters defined before: the beam height (h), the thickness (t) and the length (L). Here, parametric studies are carried out for unit cells' rotational transitions and a series of unit cells with different parameters is tested. Moreover, we have characterized the tangent slope of each force-displacement curve for the initial and rotational state. k_0 and k_1 are referred to as the tangent slope of each force-displacement curve at the points corresponding to the initial and rotational state, as illustrated in Fig. 3(a). Similarly, when varying h and L, k_0 and k_1 can also be quantified for the corresponding load-displacement curves.

3.2.1. Thickness variation

Results of the unit cells' rotational transitions with different thickness (t) are presented in Fig. 3(a)–(c). Fig. 3(b) shows the change of F_{max} and F_{min} versus the variation of thickness. The minor deviations between experimental and numerical results are mainly attributed to manufacturing imperfections and local defects introduced during printing. It can be seen that F_{max} is increasing dramatically with respect to the change of thickness. This is due to the fact that both bending and compression energy of the unit cell increase monotonically with the increasing of t. The variation of minimum force (F_{min}) shows a small distinction as compared to that of F_{max}. Nevertheless, it is clear that when thickness is large, the corresponding F_{min} is a positive value, which means that the structure switches back to the initial state after removal of load. This is verified in FEA (shown in Fig. 3(b)) as well as experimental demonstrations such that unit cells with small t can realize self-stable rotational states while the unit with a thickness of 1.6 mm recovers back to the initial state upon removing the load (see Supplementary Video). This shows that t is crucial for rotational stability. Moreover, results in Fig. 3(c) show that the stiffness k_0 increases monotonically when t increases. However, k_1 first increases and then dramatically decreases when t is larger than 1.38 mm in this case. This indicates that the unit cell possesses tunable stiffness, which is related to its multiple stable states.

3.2.2. Length variation

Fig. 3 (d)–(f) display the influence of the beam length (L) on rotational properties while keeping other parameters unchanged. Results show that the value of F_{max} decreases with the increase of L, while F_{min} is increasing. Similar characteristics can be captured for both k_0 and k_1 that stiffness decreases when L is increased. Furthermore, it can be seen from Fig. 3(e) that the slope of the F_{min} curve gradually decreases. As compared to the effect of t, the beam length L has minor effects on the sign of F_{min}, which is still negative despite its magnitude is decreasing. Similarly, it was also found that L has minor influence on the sign of F_{min} of translational transitions [55]. It should be mentioned that this effect of L is only applicable for shallow and thin beams, where L is much larger than h and t.

3.2.3. Height variation

Results presented in Fig. 3(g)–(i) show that the beam height (h) has a different influence on the rotational behavior. The effect can be summarized as: *i*) F_{max} increases with an increasing of h, similar to the effect of t; differently, the F_{max} curve gradually increases in a linear manner (see Fig. 3(h)). *ii*) When enlarging h, F_{min} and the slope of F_{min} curve decrease, as shown in Fig. 3(h). *iii*) The changes of k_0 and k_1 exhibit different characteristics. The k_0 increases with increasing h in a proportional manner, while the k_1 increases with a small rate of change. This relation results from the energy variation of the unit cell, where the height (h) influences both initial curvature and length of the beam. Changing the geometric parameters can control the variation of elastic energy during deformations. The tunability of stiffness offers the potential to tune structures' dynamic behavior by switching into different stable states.

4. Design criteria for rotational states

From the previous section, it is found that geometric parameters (t, L, h) affect rotational transitions in different manners. With changing these parameters, the rotational response can shift from stabilizing at the rotational states ($F_{min} < 0$) to switching back to the initial state (no rotational states, $F_{min} > 0$). In order to explore the design space for realizing rotational stable states, we present an analytical investigation of the rotational behavior on the basis of parameters defined before.

4.1. Model formulation

The theoretical analysis is established for the unit cell's rotational transitions by combining buckling modes of the beam elements. It has

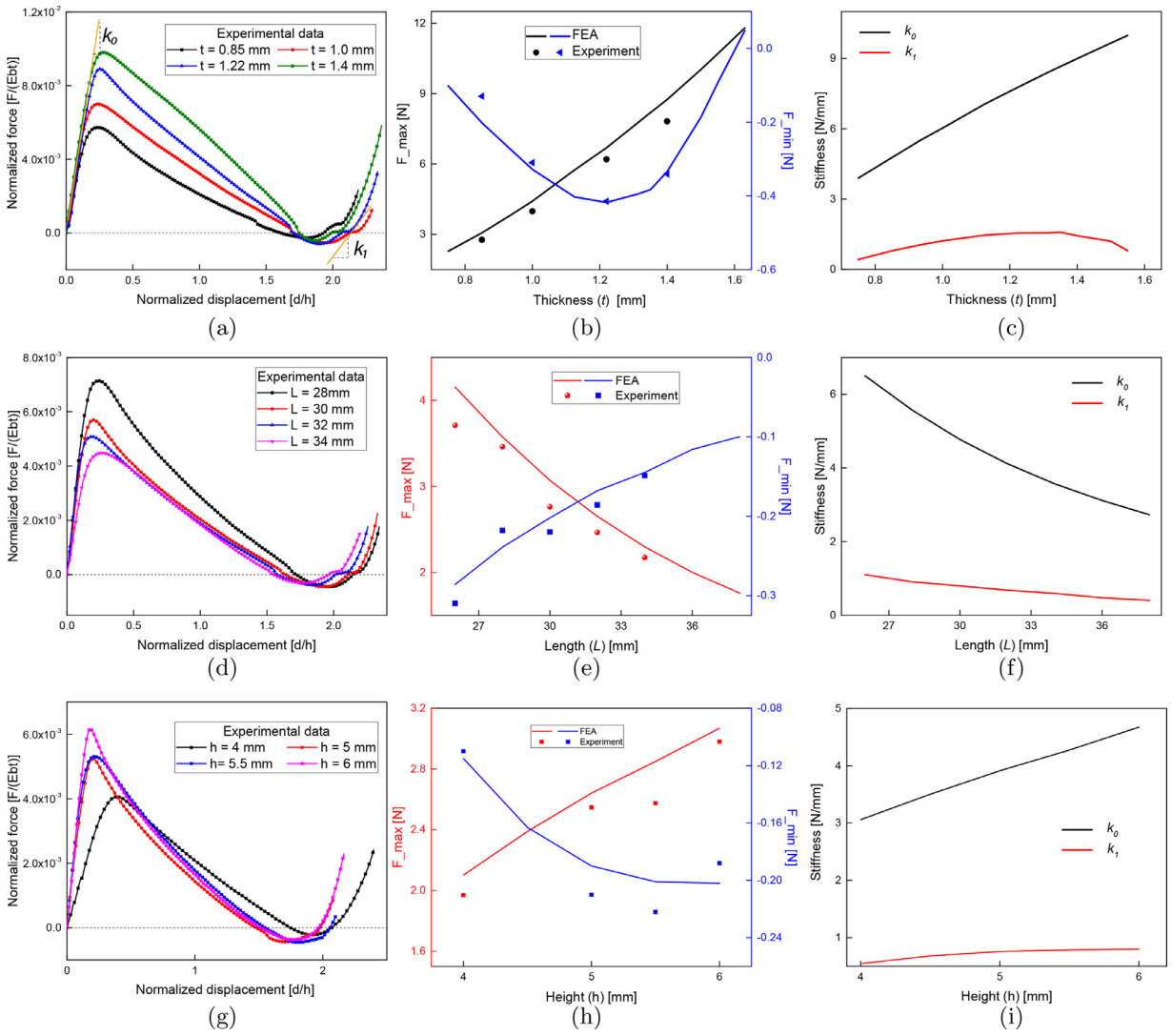

Fig. 3. The influence of t, h, and L on rotational responses. (a)–(c): The effect of t on rotational transitions. (a) shows experimentally measured load-displacement curves for specimens with different thickness. k_0 and k_1 are defined as the slope of tangent line (orange color) at two stable locations (the initial and rotational state). (b) presents F_{max} and F_{min} of force-displacement curves as a function of thickness. The positive sign of F_{min} indicates that the rotational stable state does not exist. (c) represents the change of k_0 and k_1 when varying thickness in FEA. (d)–(f): The effect of L on rotational transitions. (g)–(i): The effect of h on rotational transitions.

been reported in literature that utilizing buckling modes can provide a good estimation of load-displacement responses for the snapping beams [35,56–58]. Here, since the unit cell undergoes both symmetric and asymmetric deformations (see Fig. 4(a)), dominant modes (symmetric Mode 1 and asymmetric Mode 2) are employed to construct displacement fields, as displayed in Fig. 4(b). Based on the assumed displacement field, the potential energy is then formulated to derive the governing equations.

4.1.1. Elastic energy for a single beam

We first derive energy formulas for each single clamped-clamped pre-shaped curved beam illustrated in Fig. 4(d), and then formulate the model for the unit cell. The beam's geometric parameters are depicted in Fig. 4(d), with $X-Y$ coordinate defined. According to Euler Bernoulli equations [59], the first and second buckling modes of a straight beam that is axially compressed to buckle are given as:

$$Y_1 = 1 - cos\left(N_1 \frac{x}{L}\right) \quad \text{with} \quad N_1 = 2\pi \tag{2}$$

$$Y_2 = 1 - 2\frac{x}{L} - cos\left(N_2 \frac{x}{L}\right) + \frac{2}{N_2} sin\left(N_2 \frac{x}{L}\right) \tag{3}$$

where N_2 is the first positive solution of equation $\tan(N_2/2) = N_2/2$. The deformed beam shape (Y) under a given load is described as:

$$Y = A_1 Y_1 + A_2 Y_2 \quad \text{and} \quad Y_0 = \frac{h}{2} Y_1 \tag{4}$$

$$d = Y_0 - Y \tag{5}$$

where Y_0 is the initial beam shape and d is the displacement of the beam. A_1 and A_2 are unknown coefficients, which need to be solved on the basis of the principle of minimum energy. The elastic energy for the curved beam is obtained, which includes bending energy (U_b) and compression energy (U_c). The bending and compression energy is derived respectively by:

$$U_b = \frac{EI}{2} \int_0^L \left(\frac{d^2Y}{dx^2} - \frac{d^2Y_0}{dx^2} \right)^2 dx \quad \text{where} \quad I = \frac{bt^3}{12}, \tag{6}$$

$$U_c = \frac{Ebt(\Delta s)^2}{2L} \quad \text{and} \quad \Delta s = s - s_0 \tag{7}$$

Here, s is the beam's total length at any position, while s_0 is the beam's initial length. Assuming small deformations, s can be approxi-

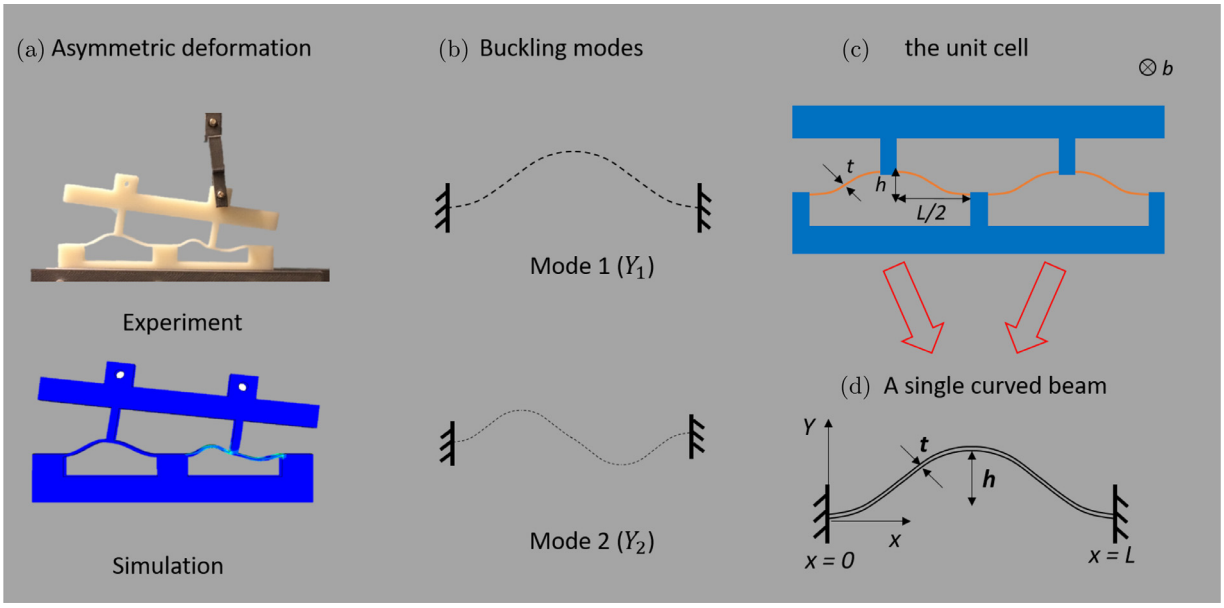

Fig. 4. Modeling a single beam based on buckling modes. (a) The rotational transitions observed in both experiments and FEA show evident asymmetric deformation modes. (b) The first two buckling modes (Mode 1 and 2) for a clamped-clamped beam. These modes are employed as bases to approximate the displacement field. (c) Geometry of the unit cell. (d) Illustration of a single curved beam. Each beam of the unit cell is modeled as a single beam. Based on the X-Y coordinate in the figure, the first two buckling modes are described by function Y_1 and Y_2, respectively.

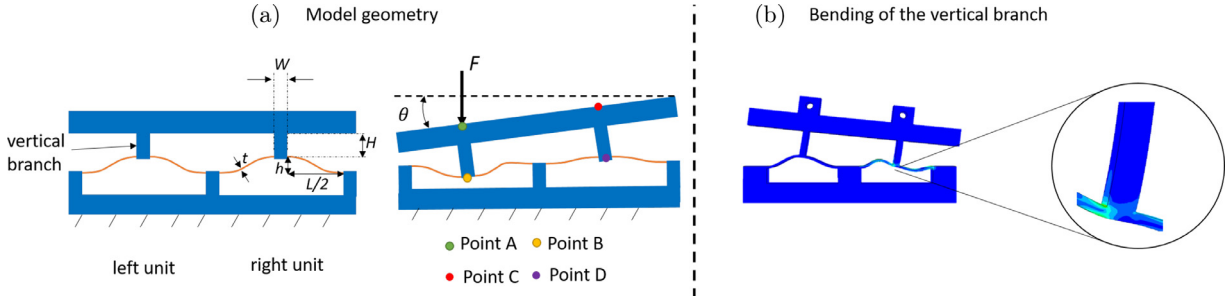

Fig. 5. Model the rotational deformation of the unit cell. (a) Unit cell's geometry and predefined parameters. b is the out-of-plane dimension. (b) As observed, the vertical branch is bent during rotational transitions. The associated bending energy is taken into account when calculating the total potential energy of the system.

mated as:

$$s = \int_0^L \sqrt{1+\left(\frac{dY}{dx}\right)^2}\,dx \approx \int_0^L \left[1+\frac{1}{2}\left(\frac{dY}{dx}\right)^2\right]dx, \tag{8}$$

By combining Eqs. (7) and (8), U_b and U_c can be expressed as a function of A_1 and A_2, as shown in Eqs. (9)–(10). C_1,C_2,D_1,D_2 are constants, which follow from integrations along the x axis (see Supporting Material).

$$U_b = \frac{EI}{2L^3}\left[(-h\boldsymbol{A_1} + \boldsymbol{A_1^2} + \frac{h^2}{4})C_1 + \boldsymbol{A_2^2}C_2\right] \tag{9}$$

$$U_c = \frac{EA}{8L^3}\left\{ D_1^2\boldsymbol{A_1^4} + D_2^2\boldsymbol{A_2^4} + 2D_1D_2\boldsymbol{A_1^2}\boldsymbol{A_2^2} - \frac{h^2D_1^2}{2}\boldsymbol{A_1^2} - \frac{h^2D_1D_2}{2}\boldsymbol{A_2^2} + \frac{h^4D_1^2}{16}\right\} \tag{10}$$

4.1.2. Model the unit cell

Based on the derived formulation for a single beam, we now build the model for the unit cell which is composed of two pre-shaped beams connected by frames. The geometric parameters of the unit cell are illustrated in Fig. 5(a), where each beam's shape (represented as left and right unit) is modeled using the formula derived in Section 4.1.1. Specifically, each beam's geometry is determined by t, L, and h, which are the same notations used before. The vertical branch denoted in Fig. 5(a) represents the vertical part of the upper frame, with dimensions depicted as H and W. As observed in simulation, this vertical branch is bent during loading, as shown in Fig. 5(b). Therefore, the bending energy of the branch is taken into account in the following energy formulation. The unit is compressed by a load (F) at point A, as illustrated in Fig. 5(a). The angle of the upper frame is depicted as θ.

a. Kinematics

As discussed in the previous section, the left and right beam's shape (denoted as Y^L and Y^R) can be described as:

$$Y^L = {A_1}^L Y_1 + {A_2}^L Y_2 \quad \text{and} \quad Y^R = {A_1}^R Y_1 + {A_2}^R Y_2 \tag{11}$$

where Y_1 and Y_2 are the first two buckling modes, as defined before. ${A_1}^L$,${A_2}^L$,${A_1}^R$,${A_2}^R$ are unknown factors, which need to be solved. The displacement of each beam's midpoint (Point B and D), denoted as d^B and d^D, can be expressed as:

$$d^B = h - 2{A_1}^L, \quad d^D = h - 2{A_1}^R \tag{12}$$

Kinematic relationship between the vertical displacement of Point A (denoted as d^A) and C (denoted as d^C) is presented in Eqs. (13). The relation between ${A_1}^L$ and ${A_1}^R$ is derived, as shown in Eqs. (14).

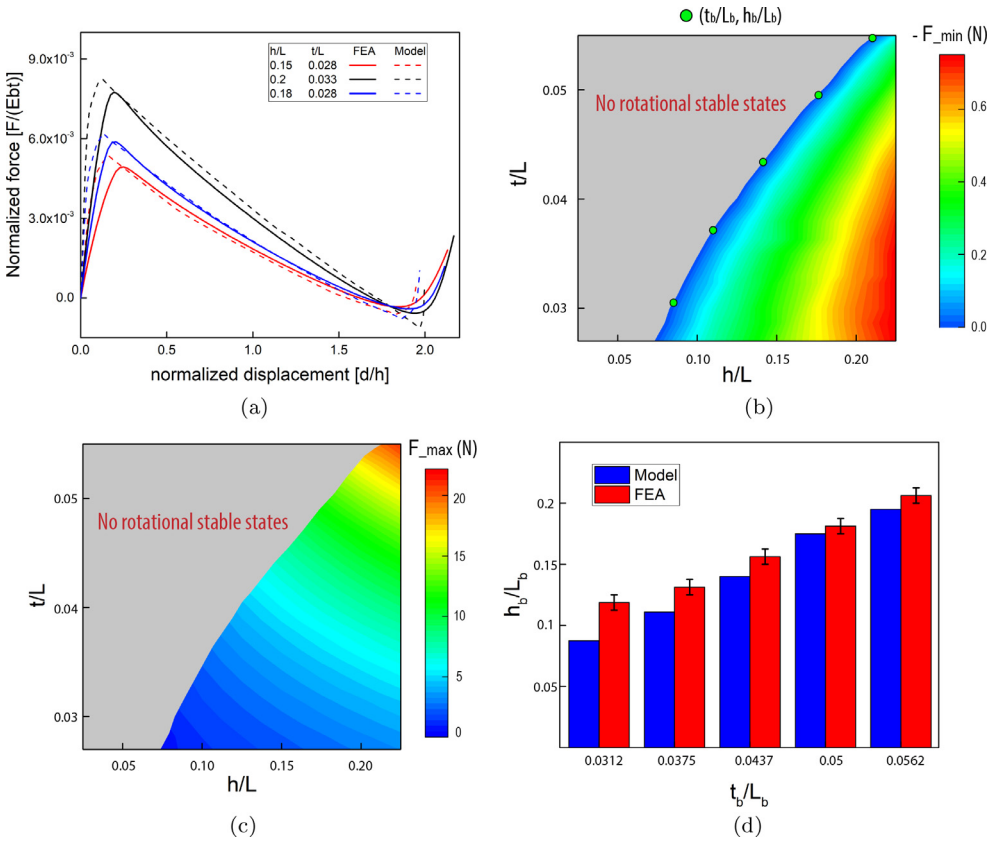

Fig. 6. Identification of design space for rotational stable states as a function of t/L and h/L. (a) Theoretical predicted load-displacement curves for the units with different parameters. FEA results are used as references. (b) With changing t/L and h/L, the design space for rotational stable states is identified by the model. The grey area represents the situation, in which there are no rotational stable states; the colored region represents the range of parameter values, for which the structure does have rotational stable states. Green dots are specific data points (denoted as t_b/L_b and h_b/L_b) along the boundary. (c) The change of F_{max} with respect to t/L and h/L. (d) The t_b/L_b and h_b/L_b predicted by the model and FEA, respectively. The error bars marked in FEA represent that the simulated h_b/L_b that is exactly corresponding to $F_{min} = 0$ is located between the upper and lower limits.

$$d^A = d^C + L_x sin(\theta) \tag{13}$$

$$A_1{}^L = A_1{}^R - \frac{L_x sin(\theta)}{2} \approx A_1{}^R - \frac{L_x \theta}{2} \tag{14}$$

L_x is the distance between Point A and C, which is a constant value.

b. Potential energy

The total potential energy for the unit under the point-force loading is formulated to obtain the four unknown coefficients ($A_1{}^L$,$A_2{}^L$,$A_1{}^R$,$A_2{}^R$). There are four energy contributions, which are the bending energy of left and right beam ($U_b{}^L$ and $U_b{}^R$), the compression energy of left and right beam ($U_c{}^L$ and $U_c{}^R$), the bending energy of vertical branch (U_v) and potential energy (U_e).

$U_b{}^L$,$U_c{}^L$ can be derived by substituting $A_1{}^L$, $A_2{}^L$ for A_1 and A_2 in Eqs. (9) and (10) (see Supporting Material). Similarly, by combining Eqs. (9), (10) and (14), we can get the expression of $U_b{}^R$, $U_c{}^R$, as a function of $A_1{}^L$, $A_2{}^R$ and θ. Finally, there are four independent unknown variables ($A_1{}^L$, $A_2{}^L$, θ, $A_2{}^R$) in the governing equations. Moreover, the bending energy of the vertical branch can be expressed as:

$$U_v = \frac{EI_B\left(\frac{A_2^L C_s}{L} + \theta\right)^2}{2H} + \frac{EI_B\left(\frac{A_2^R C_s}{L} + \theta\right)^2}{2H} \tag{15}$$

where EI_B represents the bending stiffness of the vertical beam and C_s is a constant value, as shown in the Supporting Material. The potential energy, associated to applied force, is simply:

$$U_e = -Fd^A \tag{16}$$

Finally, the total potential energy is:

$$U_{tot} = U_b{}^L + U_c{}^L + U_b{}^R + U_c{}^R + U_v + U_e \tag{17}$$

and the governing equations are obtained by taking the derivative of U_{tot} with respect to four variables ($A_1{}^L$,$A_2{}^L$,θ,$A_2{}^R$). The equations are then solved numerically by giving a range of F inputs. Consequently, the corresponding load-displacement ($F - d^A$) curves can be extracted.

4.2. Results of the analytical model

The corresponding load-displacement curves predicted by the analytical model are presented in Fig. 6(a). It can be seen that the model gives a good approximation of rotational snap-through characteristics that are observed in FEA. Specifically, the theoretical results exhibit the same slope as that of FEA in the negative stiffness phase. This can be explained by the fact that snapping behavior is mainly determined by the asymmetric Mode 2, which has been used as a modal basis in the analytical formulation. Meanwhile, it is shown that the deformed stable position of the rotational state is well predicted by the model. As compared to the FEA results, higher stiffness are observed in this model's predictions. The differences are mainly caused by two factors. First, the theoretical model does not consider high order buckling modes since using dominant modes already allow to capture the characteristic of snap-through deformation at the snapping phase, which is our focus in this study. Second, the model is based on small deformation hypothesis, as reflected in the energy formulations.

The design criterion for the rotational stability is presented in Fig. 6(b), based on two non-dimensional quantities (h/L and t/L). The grey region in the figure is corresponding to the case that the structure cannot stabilize at the deformed rotational state, where F_{min} is a positive value. The colored region means that the unit is able to achieve rotational stable states by setting proper h/L and t/L. Geometrical thresholds along the boundary are highlighted as green dots, which are denoted as t_b/L_b and h_b/L_b. The t_b/L_b and h_b/L_b obtained from the model are compared with FEA, as shown in Fig. 6(d). It is shown that the model is able to give a reasonable prediction of the boundary that determines the rotational states. Therefore, it allows a rapid and full identification of the design space for rotational stability before manufacturing.

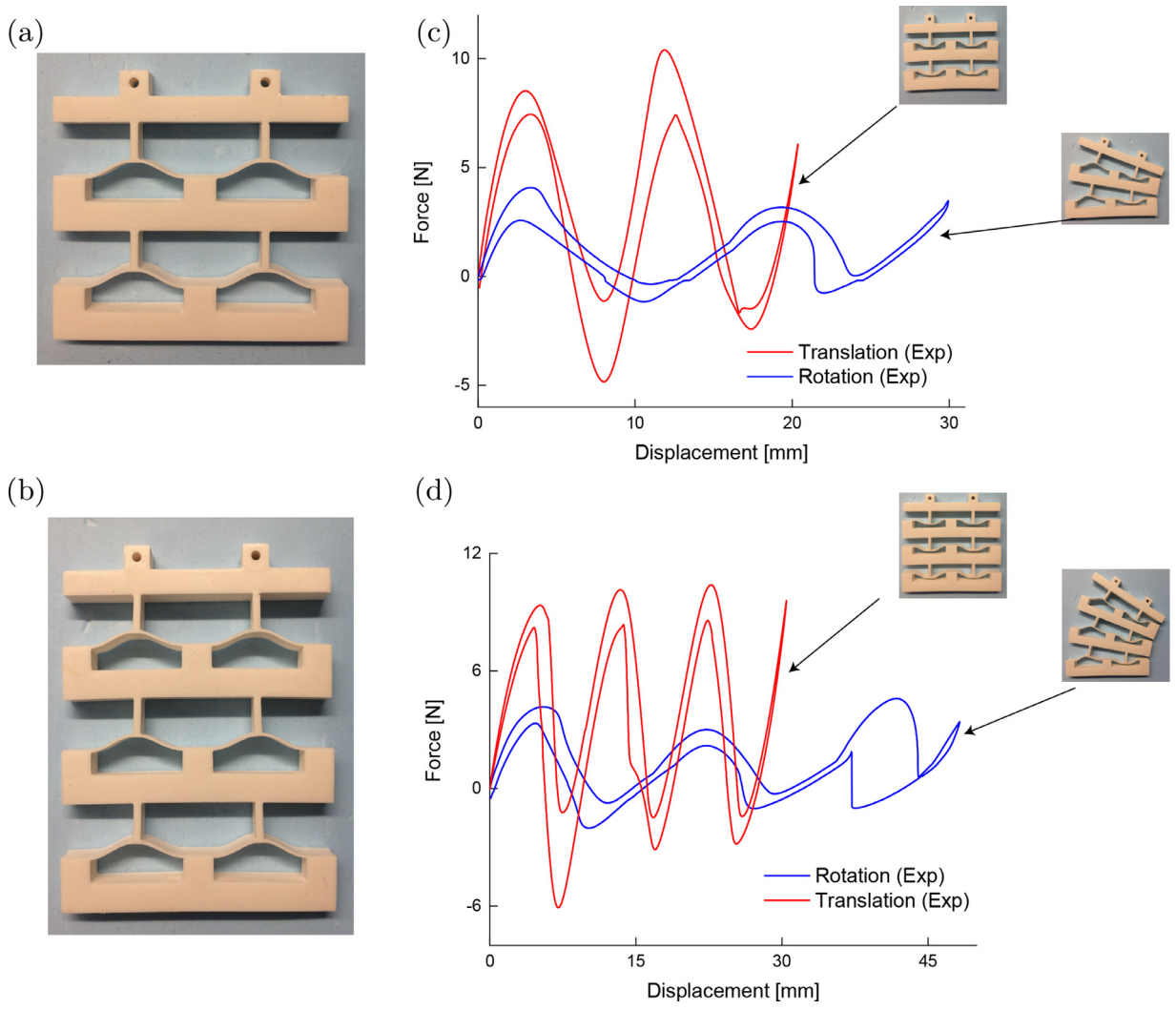

Fig. 7. 2D multi-layer metastructures with serial arrangements of unit cells. (a) A two-layer metastructure. (b) A three-layer metastructure. (c) Experimentally characterized load-displacement curves for the translational and rotational snap-through of the two-layer metastructure. The metastructure can stabilize at their deformed states, as shown in the figure. (d) Snap-through responses of the three-layer metastructures. The translational and rotational transitions are characterized respectively.

In addition, from Fig. 6(b), it can be noted that for a specified thickness, the rotational stable state can be realized when h/L of the structure is larger than the h_b/L_b. In order to reach the rotational stable state, h/L should be larger than the critical value while t/L should not exceed a specific value. It can also be interpreted in the sense that h/t should be large for achieving the rotational stable states. Besides, we explore the variation of F_{max} with respect to t/L and h/L, and results are plotted in Fig. 6(c). As compared to h/L, t/L has a more substantial influence on F_{max}. That is, the value of F_{max} increases dramatically with the change of t/L, while the change of h/L does not influence F_{max} much. Therefore, it is more paramount to change the parameter t/L when the maximal actuation force needs to be tuned to accommodate different circumstances.

5. Multi-layer metastructures with rotations

Via rationally designing the beam with specific geometric parameters, we can obtain the desired rotational states as well as the intrinsic translational states for the unit cell. By assembling such units in series, metastructures with multiple layers can be designed, which are able to exhibit large rotations and translations. To demonstrate the feasibility of the multi-layer metastructurese, we experimentally characterize their snapping transitions.

Two-layer and three-layer metastructures are displayed in Fig. 7(a)–(b). As the unit cell possesses four stable states, the printed two-layer and three-layer metastructures have 4^2 and 4^3 stable states, respectively. Here, two primary deformation modes are selected and characterized by cyclic loading. The associated load-displacement responses are plotted in Fig. 7(c)–(d), where each layer exhibits evident snap-through behavior sequentially. In Fig. 7(d), a large difference between loading and unloading during the third snapping occurs. This happens due to the fact that during uniaxial loading, the top layer of the three-layer metastructure also generates a horizontal displacement, which can not be handled by the uniaxial testing. In terms of characterizing the rotations of a metastructure with more layers, the horizontal displacement of the metastructure needs to be taken into account. The multi-stable metastructures are able to stabilize at their deformed (translational and rotational) states after removal of loads. After unloading, the metastructure can be fully reversed back to the initial state, which means that they can be reused.

More importantly, from a kinematics perspective, the proposed multi-stable structure is capable of not only providing translational but also angular movements, which enriches the structure's shape-morphing ability. As shown in Fig. 8(a), the multi-layer metastucture can exhibit different curved shapes that are enabled by the unit's rotational states,

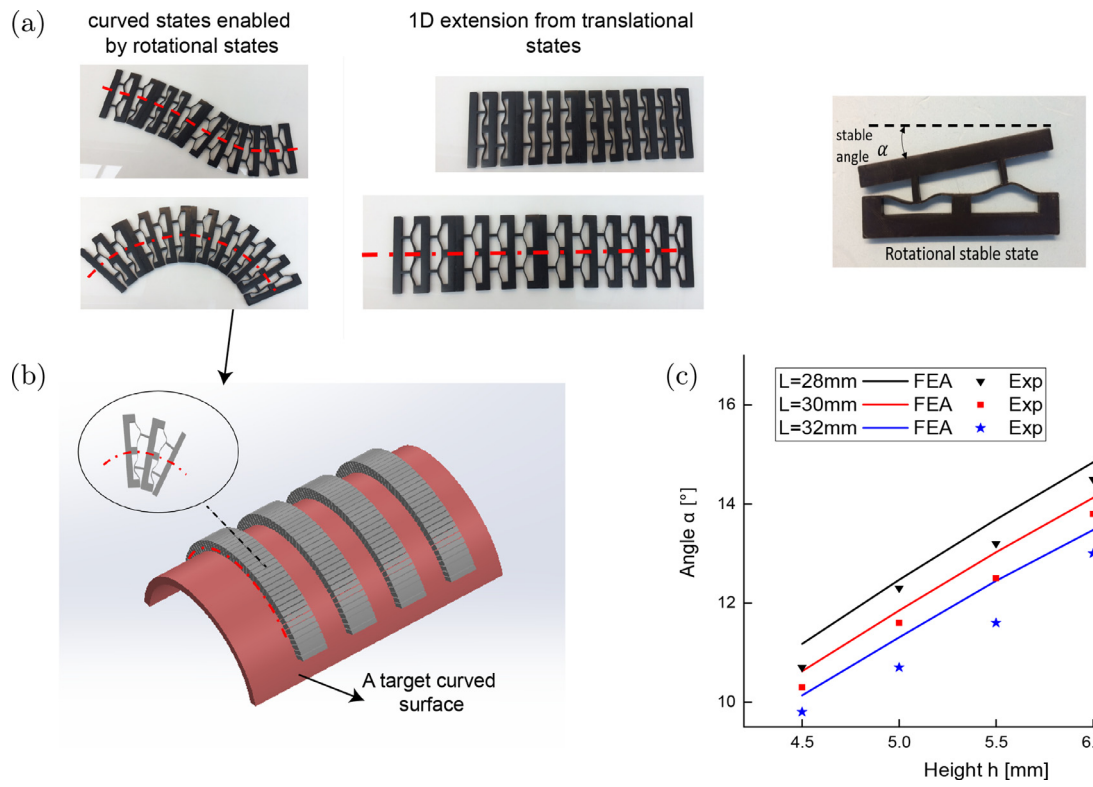

Fig. 8. Demonstrations of conformal-morphing on a curved surface based on the rotational stable states. (a) An ensemble of unit cells stacked in series. By deforming in different transition modes, it can switch to curved shapes with different curvatures. The angle α is the stable angle achieved by a single unit's rotational transitions. (b) An illustrative example of conformal morphing on a spatial free-form surface. To realize shape-matching, our deformed metastructures (grey) can deform into a curved shape to match the target curved free-form shape (red). (c) The stable angle (α) is characterized experimentally and numerically, as a function of h for different L.

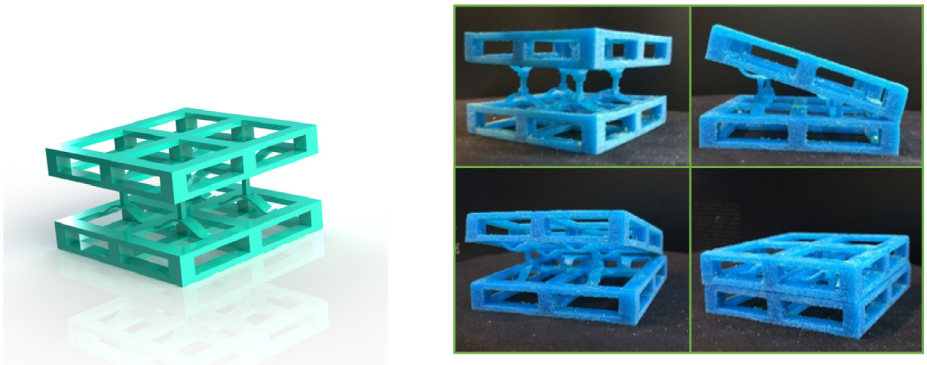

Fig. 9. 3D multi-stable metastructures with rotational states. (a) The metastructure is designed by arranging unit cells in an orthogonal pattern. (b) The fabricated prototype of the 3D metastructure. The structure is able to exhibit rotations along two directions, which result in four rotational stable states.

aside from the 1D extension shown in Fig. 8(a). Such deformed curved states can be useful for shape morphing, in which the ability to deform into curved shapes is normally needed. An illustrative example is shown in Fig. 8(b), where conformal morphing can be realized. To match a target curved shape (denoted in red), it is possible to make the metastructures (marked in grey) deform to fit into the shape of the target curved shape via controlling the rotational stable state of each unit cell, while the translational states of the presented structures shown in Fig. 8(a) cannot realize the morphing behavior to match the curved surface. The largest rotational angle can be calculated as $n\alpha$, where n is the number of layers. Since the beam height (h) and length (L) have more substantial effects on α than the thickness (t), we plot the change of α with the variation of h and L, as shown in Fig. 8(c). It can be seen that α increases approximately in a linear manner with the increasing of the beam height. With larger h and L, the achievable angle α can be enlarged. Then, rotational angles can be programmed by adjusting the number of layers and the geometry of the unit cells. Meanwhile, it should also be noted that a large α requires a large distance between the upper and bottom frame. Here, we observe that a large h will lead to contact between the upper and bottom frame when reaching the rotational state (see Supporting Material). Therefore, when designing the structure with a large h, the contact issue should be considered.

In addition, we demonstrate the rotations of a 3D multi-stable metastructure. This metastructure is shown in Fig. 9(a), and is designed with two units placed in an orthogonal pattern. It is fabricated using a poly-jet based multi-material printer (Objet350 Connex 3). From Fig. 9(b), it can be seen that this 3D metastructure is able to realize rotations along two directions, which is an extension of 2D structures. The rotational states in Fig. 9(b) can be seen as the deformations of two rows of 2D unit cells arranged in parallel. Therefore, it can be expected that the magnitude

of this 3D structure's rotational force-displacement response, including force thresholds and stiffness, should be two times as large as a single 2D unit cell with the same length scales. This 3D structure can be further extended to design bending actuators by stacking more unit cells. Overall, the design of 3D structure here paves the way for forming 3D deployable structures by patterning structures in x, y, z directions.

6. Conclusions

In this work, the rotational stable states of multi-stable beam-type metastructures have been presented, apart from the expected translational states. Both translational and rotational transitions exhibit negative stiffness (snap-through) behavior while the rotational transition exhibits more evident asymmetric characteristics as compared to the counterpart of translations. The parameters, including the beam height (h), thickness (t) and span (L), have been found paramount for rotational stability. Moreover, the criterion for reaching rotational states is established through a theoretical investigation. The proposed model, validated by finite element simulations, effectively predicts the rotational snap-through transitions in the negative stiffness interval and captures thresholds of h/L and t/L. It is shown that for realizing rotational states, h/L should be larger than critical values while t/L needs to be small, and t/L is more influential than h/L for tuning the maximum force of rotational transitions. This criterion serves as a guideline to tailor rotational snap-though behavior such as controlling force thresholds. Finally, we demonstrate the large rotations of metastructures with fabricated two- and three-dimensional metastructures, where the rotational stable states can be programmed by serially assembling units along multiple directions. With the proper units arrangement and design, the proposed multi-stable metastructures with rotational states can open up new opportunities for designing adaptive structures.

Declaration of Competing Interest

The authors declare that they have no known competing financial interests or personal relationships that could have appeared to influence the work reported in this paper.

CRediT authorship contribution statement

Yong Zhang: Conceptualization, Methodology, Validation, Investigation, Writing - original draft, Visualization. **Marcel Tichem:** Writing - review & editing, Supervision. **Fred van Keulen:** Methodology, Writing - review & editing, Supervision.

Acknowlgedgments

Y. Zhang would like to thank China Scholarship Council (CSC NO. 201606120015) for the financial support. Bradley But at Department of Precision and Microsystems Engineering of Delft University of Technology is acknowledged for the discussion on printing.

Appendix A. Supporting Material

Supplementary document: the detailed derivation of the proposed analytical model and the contact between the uppper and bottom frame when increasing h.

Supplementary video: With changing thickness, the unit cells exhibit rotational states and do not have rotational states, respectively.

Supplementary material associated with this article can be found, in the online version, at 10.1016/j.ijmecsci.2020.106172

References

[1] Zheng X, Lee H, Weisgraber TH, Shusteff M, DeOtte J, Duoss EB, et al. Ultralight, ultrastiff mechanical metamaterials. Science 2014;344(6190):1373–7.
[2] Schaedler TA, Jacobsen AJ, Torrents A, Sorensen AE, Lian J, Greer JR, et al. Ultralight metallic microlattices. Science 2011;334(6058):962–5.
[3] Meza LR, Das S, Greer JR. Strong, lightweight, and recoverable three-dimensional ceramic nanolattices. Science 2014;345(6202):1322–6.
[4] Schaedler TA, Carter WB. Architected cellular materials. Annual Review of Materials Research 2016;46:187–210.
[5] Bauer J, Meza LR, Schaedler TA, Schwaiger R, Zheng X, Valdevit L. Nanolattices: an emerging class of mechanical metamaterials. Advanced Materials 2017;29(40):1701850.
[6] Ren X, Das R, Tran P, Ngo TD, Xie YM. Auxetic metamaterials and structures: A review. Smart materials and structures 2018;27(2):023001.
[7] Wang H, Zhang Y, Lin W, Qin Q-H. A novel two-dimensional mechanical metamaterial with negative poissons ratio. Computational Materials Science 2020;171:109232.
[8] Lakes RS. Negative-poisson's-ratio materials: auxetic solids. Annual review of materials research 2017;47:63–81.
[9] Takenaka K. Negative thermal expansion materials: technological key for control of thermal expansion. Science and Technology of Advanced Materials 2012;13(1):013001.
[10] Wang Q, Jackson JA, Ge Q, Hopkins JB, Spadaccini CM, Fang NX. Lightweight mechanical metamaterials with tunable negative thermal expansion. Physical review letters 2016;117(17):175901.
[11] Ai L, Gao X-L. Three-dimensional metamaterials with a negative poisson's ratio and a non-positive coefficient of thermal expansion. International Journal of Mechanical Sciences 2018;135:101–13.
[12] Zhu H, Fan T, Peng Q, Zhang D. Giant thermal expansion in 2d and 3d cellular materials. Advanced Materials 2018;30(18):1705048.
[13] Bobbert F, Janbaz S, van Manen T, Li Y, Zadpoor A. Russian doll deployable meta-implants: Fusion of kirigami, origami, and multi-stability. Materials & Design 2020:108624.
[14] Choi J, Lakes R. Analysis of elastic modulus of conventional foams and of re-entrant foam materials with a negative poisson's ratio. International Journal of Mechanical Sciences 1995;37(1):51–9.
[15] Zadpoor AA. Meta-biomaterials. Biomaterials Science 2020;8(1):18–38.
[16] Bobbert F, Janbaz S, Zadpoor A. Towards deployable meta-implants. Journal of Materials Chemistry B 2018;6(21):3449–55.
[17] Schaffner M, Faber JA, Pianegonda L, Rühs PA, Coulter F, Studart AR. 3d printing of robotic soft actuators with programmable bioinspired architectures. Nature communications 2018;9(1):878.
[18] Gorissen B, Melancon D, Vasios N, Torbati M, Bertoldi K. Inflatable soft jumper inspired by shell snapping. Science Robotics 2020;5(42).
[19] Zhao X, Duan G, Li A, Chen C, Zhang X. Integrating microsystems with metamaterials towards metadevices. Microsystems & nanoengineering 2019;5(1):1–17.
[20] Hu N, Burgueño R. Buckling-induced smart applications: recent advances and trends. Smart Materials and Structures 2015;24(6):063001.
[21] Bertoldi K, Vitelli V, Christensen J, van Hecke M. Flexible mechanical metamaterials. Nature Reviews Materials 2017;2(11):17066.
[22] Oliveri G, Overvelde JT. Inverse design of mechanical metamaterials that undergo buckling. Advanced Functional Materials 2020;30(12):1909033.
[23] Kim Y, Yuk H, Zhao R, Chester SA, Zhao X. Printing ferromagnetic domains for untethered fast-transforming soft materials. Nature 2018;558(7709):274–9.
[24] Janbaz S, Bobbert F, Mirzaali M, Zadpoor A. Ultra-programmable buckling-driven soft cellular mechanisms. Materials Horizons 2019;6(6):1138–47.
[25] Correa DM, Klatt T, Cortes S, Haberman M, Kovar D, Seepersad C. Negative stiffness honeycombs for recoverable shock isolation. Rapid Prototyping Journal 2015;21(2):193–200.
[26] Pan F, Li Y, Li Z, Yang J, Liu B, Chen Y. 3d pixel mechanical metamaterials. Advanced Materials 2019;31(25):1900548.
[27] Bertoldi K. Harnessing instabilities to design tunable architected cellular materials. Annual Review of Materials Research 2017;47:51–61.
[28] Yang D, Mosadegh B, Ainla A, Lee B, Khashai F, Suo Z, et al. Buckling of elastomeric beams enables actuation of soft machines. Advanced Materials 2015;27(41):6323–7.
[29] Rafsanjani A, Bertoldi K, Studart AR. Programming soft robots with flexible mechanical metamaterials. Science Robotics 2019;4(29).
[30] Simitses G, Hodges DH. Fundamentals of structural stability. Butterworth-Heinemann; 2006.
[31] Yang H, Ma L. Multi-stable mechanical metamaterials with shape-reconfiguration and zero poisson's ratio. Materials & Design 2018;152:181–90.
[32] Che K, Yuan C, Qi HJ, Meaud J. Viscoelastic multistable architected materials with temperature-dependent snapping sequence. Soft matter 2018;14(13):2492–9.
[33] Tan X, Chen S, Zhu S, Wang B, Xu P, Yao K, et al. Reusable metamaterial via inelastic instability for energy absorption. International Journal of Mechanical Sciences 2019;155:509–17.
[34] Hua J, Lei H, Zhang Z, Gao C, Fang D. Multistable cylindrical mechanical metastructures: Theoretical and experimental studies. Journal of Applied Mechanics 2019:1–27.
[35] Che K, Yuan C, Wu J, Qi HJ, Meaud J. Three-dimensional-printed multistable mechanical metamaterials with a deterministic deformation sequence. Journal of Applied Mechanics 2017;84(1):011004.
[36] Yang H, Ma L. 1d to 3d multi-stable architected materials with zero poisson's ratio and controllable thermal expansion. Materials & Design 2020;188:108430.
[37] Meaud J, Che K. Tuning elastic wave propagation in multistable architected materials. International Journal of Solids and Structures 2017;122:69–80.
[38] Wu L, Xi X, Li B, Zhou J. Multi-stable mechanical structural materials. Advanced Engineering Materials 2018;20(2):1700599.

[39] Sun S, An N, Wang G, Li M, Zhou J. Snap-back induced hysteresis in an elastic mechanical metamaterial under tension. Applied Physics Letters 2019;115(9):091901.
[40] Ha CS, Lakes RS, Plesha ME. Design, fabrication, and analysis of lattice exhibiting energy absorption via snap-through behavior. Materials & Design 2018;141:426–37.
[41] Tan X, Wang B, Chen S, Zhu S, Sun Y. A novel cylindrical negative stiffness structure for shock isolation. Composite Structures 2019;214:397–405.
[42] Frenzel T, Findeisen C, Kadic M, Gumbsch P, Wegener M. Tailored buckling microlattices as reusable light-weight shock absorbers. Advanced Materials 2016;28(28):5865–70.
[43] Restrepo D, Mankame ND, Zavattieri PD. Phase transforming cellular materials. Extreme Mechanics Letters 2015;4:52–60.
[44] Shan S, Kang SH, Raney JR, Wang P, Fang L, Candido F, et al. Multistable architected materials for trapping elastic strain energy. Advanced Materials 2015;27(29):4296–301.
[45] Chen T, Bilal OR, Shea K, Daraio C. Harnessing bistability for directional propulsion of soft, untethered robots. Proceedings of the National Academy of Sciences 2018;115(22):5698–702.
[46] Chen T, Mueller J, Shea K. Integrated design and simulation of tunable, multi-state structures fabricated monolithically with multi-material 3d printing. Scientific reports 2017;7:45671.
[47] Santer M, Pellegrino S. Concept and design of a multistable plate structure. Journal of Mechanical Design 2011;133(8):081001.
[48] Pontecorvo ME, Barbarino S, Murray GJ, Gandhi FS. Bistable arches for morphing applications. Journal of Intelligent Material Systems and Structures 2013;24(3):274–86.
[49] Ren C, Li Q, Yang D. Quasi-static and sound insulation performance of a multifunctional cylindrical cellular shell with bidirectional negative-stiffness metamaterial cores. International Journal of Mechanical Sciences 2020:105662.
[50] Liu X, Lamarque F, Doré E, Pouille P. Multistable wireless micro-actuator based on antagonistic pre-shaped double beams. Smart Materials and Structures 2015;24(7):075028.
[51] Che K, Rouleau M, Meaud J. Temperature-tunable time-dependent snapping of viscoelastic metastructures with snap-through instabilities. Extreme Mechanics Letters 2019;32:100528.
[52] Yang H, Ma L. Multi-stable mechanical metamaterials by elastic buckling instability. Journal of Materials Science 2019;54(4):3509–26.
[53] Vangbo M, Bäcklund Y. A lateral symmetrically bistable buckled beam. Journal of Micromechanics and Microengineering 1998;8(1):29.
[54] Marlow R. A general first-invariant hyperelastic constitutive model. Constitutive Models for Rubber 2003:157–60.
[55] Alturki M, Burgueño R. Multistable cosine-curved dome system for elastic energy dissipation. Journal of Applied Mechanics 2019;86(9):091002.
[56] Qiu J, Lang JH, Slocum AH. A curved-beam bistable mechanism. Journal of microelectromechanical systems 2004;13(2):137–46.
[57] Cleary J, Su H-J. Modeling and experimental validation of actuating a bistable buckled beam via moment input. Journal of Applied Mechanics 2015;82(5):051005.
[58] Camescasse B, Fernandes A, Pouget J. Bistable buckled beam: Elastica modeling and analysis of static actuation. International Journal of Solids and Structures 2013;50(19):2881–93.
[59] Timoshenko SP, Gere JM. Theory of elastic stability. Courier Corporation; 2009.